PERGAMON

International Journal of Heat and Mass Transfer 45 (2002) 3771–3780

International Journal of HEAT and MASS TRANSFER

www.elsevier.com/locate/ijhmt

Contact angles and interface behavior during rapid evaporation of liquid on a heated surface

Satish G. Kandlikar *, Mark E. Steinke

Mechanical Engineering Department, Rochester Institute of Technology, Rochester, NY 14623, USA

Received 18 July 2001; received in revised form 16 February 2002

Abstract

Photographic observations of the boiling phenomena have played an important role in gaining insight into the boiling mechanism. This paper presents a brief historical review of the available literature on the photographic studies in pool and flow boiling. This is followed by the results of the photographic studies conducted in the authors' laboratory on liquid droplets impinging on a heated surface. Liquid–vapor interface and contact line movements are observed through a high speed camera at high resolution. The effect of surface roughness and surface temperature on dynamic advancing and receding contact angles has been studied. In addition, the effects of rapid evaporation on advancing and receding contact angles, liquid–vapor interface motion, and the dryout front propagation have been investigated.

1. Introduction

Boiling phenomenon has been one of the most fascinating topics in heat transfer with the complex interactions among solid, liquid and vapor phases; the liquid–vapor interface often taking artistic forms that researchers looked intently in an effort to understand the underlying thermal effects. The experimental techniques employed in the early fifties and sixties were quite sophisticated, even by today's standards, with high speed photographs taken at frame rates of up to 40,000 frames per second. Such photography remains at the very high end of the digital photography that has revolutionized the imaging world. A good summary of the photographic studies in pool boiling and impinging droplets is given in [1,2].

Gunther [3] obtained high speed photographs at 20,000 frames per second in flow boiling and noted that the bubbles became smaller as the subcooling increased. Eventually, with an increase in heat flux, a local vapor film was formed on the heater surface leading to the critical heat flux (CHF), condition. Mattson et al. focused their study to determine whether the boundary layer separation was the cause for the transition to the CHF condition. They noted that "There were no macroscopic flow pattern changes that could be characterized as abrupt or violent, and there were no oscillations in (a) bubble flow trajectories above the DNB location, (b) slope of the bubble boundary layer near the DNB location, and (c) velocity and trajectory of the vapor. None of these changes was observed." In light of these observations, it may be concluded that CHF condition is a local phenomenon initiated by conditions existing in the immediate vicinity of the heater surface.

A number of studies have been conducted to obtain photographic evidence at the CHF location. Tippets [4] obtained pictures at a frame rate of 4300 frames per second in both subcooled and low quality flow boiling regions. He observed vapor streams coming from the edges of a heater ribbon close to the CHF location. Hosler [5], Kirby et al. [6], and Tong et al. [7] conducted photographic studies near the CHF condition. Hosler observed vapor patches developing on the heater surface just prior to CHF, Kirby et al. observed that at high subcooling and high heat fluxes, bubbles coalesced and slid along the heater surface. However, they also confirmed Gunther's [3] observation that there were no noticeable changes in the flow pattern at the CHF location. Tong [8] measured the temperatures along the length of

* Corresponding author. Tel.: +1-585-475-6728; fax: +1-585-475-7710.

E-mail address: sgkeme@rit.edu (S.G. Kandlikar).

0017-9310/02/$ - see front matter
PII: S0017-9310(02)00090-X

Nomenclature

q''_c	critical heat flux (W/m^2)
h_{fg}	heat of vaporization (J/kg)
g	gravity (m/s^2)
D	initial droplet diameter (m)
h	vertical distance the water droplet travels before impact (m)
V	velocity (m/s)
T	temperature (K)
R_a	surface roughness (m)
We	Weber number ($= \rho V^2 D/\sigma$)

Greek symbols

ρ	density (kg/m^3)
σ	surface tension (N/m)
θ	contact angle (deg)
β	contact angle (deg)
ϕ	surface inclination angle (deg)
μ	viscosity (kg/ms)

Subscripts

A	advancing
d	dynamic
g	vapor
f	liquid
lg	latent quantity
R	receding
s	surface
w	water

the heated surface in the flow direction and noted temperature fluctuations in the wall near the CHF location.

The photographic studies carried out by Chandra and Avedisian [9,10] on a droplet impinging on hot surface reveal interesting information regarding the initiation of the CHF condition. Although the liquid droplet is spreading on the heater surface, the rapid evaporation at the edges causes it to curl back with a significant increase in the contact angle. This effect increases with increasing wall temperatures. The absence of any vapor plumes near the CHF suggests that this phenomenon is highly localized at the solid–liquid–vapor contact line and is dictated by the movement of the contact line and the spreading of a vapor film as postulated by Kandlikar [2].

A very good summary of droplet behavior as it impinges on a heater surface is provided by Bernardin et al. [11]. They provide a map showing various regimes a droplet undergoes upon impingement as a function of heater surface temperature and the impinging Weber number of droplets.

Recently, Kandlikar and Steinke [12,13], and Kandlikar et al. [14] conducted photographic studies on the impinging droplets on a heated surface. The effects of surface roughness, heater surface temperature, and droplet Weber number on the interface characteristics were investigated. The present paper summarizes these results along with some additional results obtained for water droplets impinging on a heated glass surface with pictures taken from underneath the surface.

2. Advancing and receding contact angles of impinging droplets on a heated surface

Effect of surface roughness and surface temperature. As a droplet impinges on a solid surface, it spreads out under the influence of the inertia and gravitational forces. The restraining forces are due to wall shear stress and surface tension. The surface tension forces are influenced by the dynamic contact angle between the liquid and solid surface. The contact angles of the advancing liquid front are generally different from the receding liquid front.

In studying the dynamics of the impinging droplets, the following two dynamic contact angles play an important role in governing the interface characteristics:

$\theta_{A,d}$ – dynamic advancing contact angle

$\theta_{R,d}$ – dynamic receding contact angle

The dynamic contact angles are different from the equilibrium, or static, contact angles. The equilibrium advancing and receding contact angles depend on the liquid, vapor, the material of the solid surface, the surface roughness, and any surface impurities that may be present on the liquid–vapor interface or the solid surface. The equilibrium contact angle actually can lie anywhere between the equilibrium advancing and equilibrium receding contact angles. The actual value depends on the way the droplet is placed on the surface and the time duration as it affects the wetting characteristics of the solid surface. Fig. 1 shows the advancing and receding contact angles for a droplet placed on a solid surface. The advancing contact angle refers to the condition when the interface is advancing toward the vapor phase. If this angle is measured while the interface is moving, it is called as the dynamic advancing contact angle. The static advancing contact angle is measured in the present setup by tilting the unit the droplet slides off. Similarly, the receding contact angle refers to the condition when the interface slides along the solid surface moving toward the liquid phase.

The effect of surface roughness on equilibrium contact angles has been studied by Kandlikar and Steinke [12]. The surface is polished using a buffing wheel and

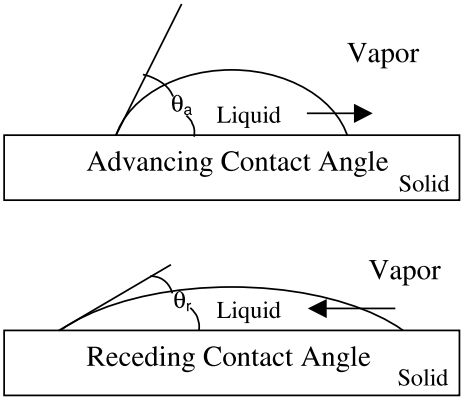

Fig. 1. Advancing and receding contact angles.

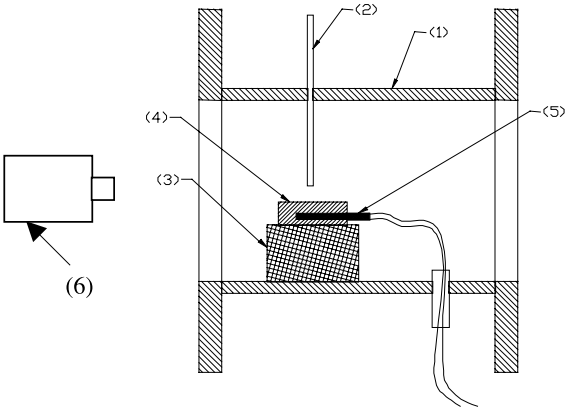

Fig. 2. Schematic of the experimental apparatus. (1) Stainless steel vessel, (2) droplet delivery system, (3) leveling stage, (4) heated copper surface, (5) cartridge heater, (6) camera. Vacuum pump and back illumination not shown.

1-μm slurry of aluminum oxide in water. The surface roughness is measured with a profile meter. The profile meter reports a roughness average value, R_a, from a continuous averaging of surface roughness heights. The profile meter has an accuracy of ±0.005 μm for the full range of measurements. The reported surface roughness values are an average of several independent measurements. The average value is within ±5% of the range of measured values. For example, a 320-grit finish on the copper surface the measured values were: 0.64, 0.62, 0.63, 0.64, and 0.64 μm. The 1-μm slurry produced an R_a value of 0.02 μm. This procedure is used to prepare the copper and stainless steel surfaces. The SilverStone® surface is tested using the factory delivered surface finish. The roughness of the SilverStone® surface was measured to be 1.35 μm. The copper surface is prepared with four different surface roughness values of 0.63, 0.32, 0.25, and 0.02 μm. The stainless steel surface is prepared with surface roughness values of 0.13, 0.07, 0.04, and 0.01 μm.

The contact angle measurement was carried out by placing the droplets on a flat, horizontal, test specimen of 25 mm diameter. A schematic of the test section is shown in Fig. 2. The test specimen and the droplet delivery system were placed inside an evacuated stainless steel chamber. Deionized (DI) water was used as the test fluid. It was heated inside the vacuum chamber and allowed to boil to remove dissolved gases. The droplets were dispensed using a surgical syringe and a precision flow control valve. The contact angle measurements were carried out in an environment of pure water vapor. The backside of the test section was illuminated using a photographic screen. The camera was placed in front of a Lexan viewing window. The distance between the camera and the test piece was 18 cm while the droplets were typically 2.8 mm in diameter. The equilibrium contact angle was measured by placing the droplet on the surface from a distance of 5 mm. The static advancing and receding contact angles were measured by gradually tilting the entire assembly on the flanges of the vacuum chamber. The angles were measured after the droplet slipped a small distance to establish the limiting values of the advancing and receding contact angles. The video images were then processed in AUTOCAD 2000 to determine the contact angle values. Repeated measurements resulted in contact angle measurements within ±3°.

Fig. 3 shows the equilibrium contact angles for stainless steel and copper surfaces as a function of surface roughness. Water droplets were placed on the surface, and the surface was tilted to generate the advancing and receding contact angle values. As seen from Fig. 3 for stainless steel, the contact angle is highest for the smoothest surface, at around 72° for $R_a = 0.02$ μm. The contact angle decreases with an increase in surface roughness. This is believed to be due to improved wetting characteristics as the surface becomes rougher.

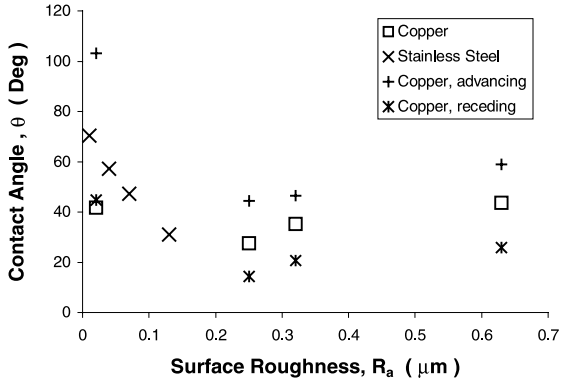

Fig. 3. Equilibrium contact angle vs. surface roughness: advancing and receding contact angles for horizontal unheated copper and stainless steel surfaces. $T_s = 22$ °C; $T_{water} = 22$ °C.

Similar behavior is observed for copper surface at low roughness values. However, as the surface roughness increases further, the contact angle starts to go up again. Larger roughness values could not be obtained with stainless steel as it was found to be very difficult to generate uniformly high roughness consistently over the entire surface. The interaction between the rough surface and the interface is quite complex, and the wetting behavior is affected by the roughness structure. It is suspected that larger roughness structures interfere with the spreading behavior, thereby increasing the contact angles. A more detailed study on the surface structure and interface forces is needed to further explain this behavior.

The equilibrium advancing and receding contact angles are also plotted in Fig. 3. The equilibrium values for copper lie between the two limits of the advancing and receding contact angles. The equilibrium advancing angle for the smoothest surface is very large, at around 102°. Both the advancing and the receding contact angles exhibit the same dependence on the surface roughness as the equilibrium contact angles.

Surface cleanliness has a major influence on the contact angles. Kandlikar et al. [15] measured the contact angles for a platinum surface that is first polished and then cleaned with acetone bath, followed by a flush with distilled water and then an air spray from a pressurized air bottle. The resulting equilibrium contact angle was measured to be 61°. The platinum surface was then once again polished and treated with a more aggressive cleaning technique using a modified RCA clean process to remove any organic materials. The bath consisted of 1 part NH_4OH, three parts H_2O_2, and 15 parts H_2O. The solution was heated to a temperature of 70 °C, and the platinum was kept submerged in it for 15 min. This was followed by a rinse with DI water. The resulting contact angle under the same experimental conditions was measured to be 22° (average of six readings, maximum variation ±1°). Extreme precautions are therefore needed in conducting the contact angle measurements.

The dynamic contact angles represent the contact angles experienced by a moving interface. Fig. 4 shows the variation of the dynamic advancing and receding contact angles with surface temperature for a copper surface.

The dynamic advancing contact angle is higher than the dynamic receding contact angle for temperatures up to about 140 °C as seen in Fig. 4. For temperatures above 140 or 150 °C, the dynamic receding angle jumps to the same value as the dynamic advancing angle. Interestingly, this is the same temperature where the liquid droplets starts experiencing critical heat flux condition leading into transition boiling.

Figs. 5 and 6 show the dynamic contact angles for stainless steel and SilverStone® surfaces. The results for

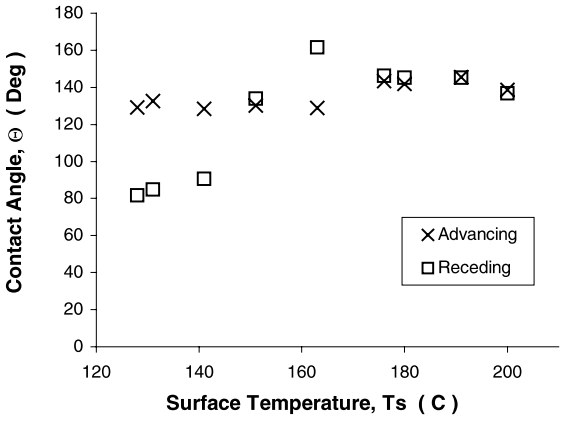

Fig. 4. Dynamic advancing and receding contact angles for a copper surface: 120 °C < T_s < 220 °C; $h = 38.1$ mm; $T_{water} = 22$ °C; $R_a = 0.02$ μm; $We = 29.4$.

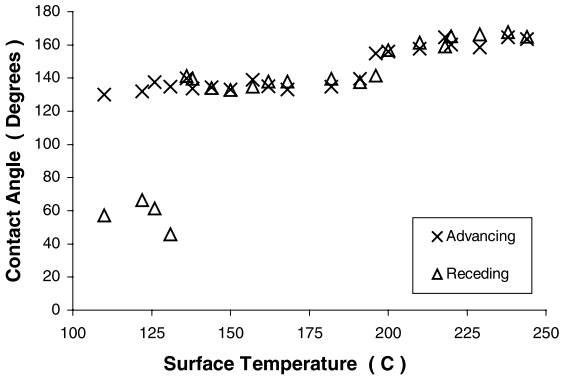

Fig. 5. Dynamic advancing and receding contact angles for a stainless steel surface: 100 °C < T_s < 250 °C; $h = 38.1$ mm; $T_{water} = 22$ °C; $R_a = 0.01$ μm; $We = 29.4$.

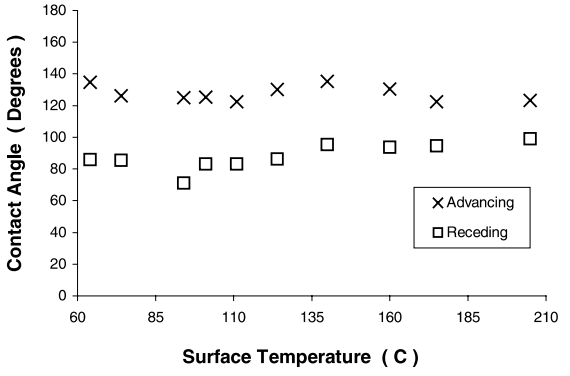

Fig. 6. Dynamic advancing and receding contact angles for a SilverStone surface: 60 °C < T_s < 210 °C; $h = 38.1$ mm; $T_{water} = 22$ °C; $R_a = 1.34$ μm; $We = 29.4$.

the stainless steel surface are identical to that for the copper surface with the dynamic receding contact angle jumping to the dynamic advancing contact angle at around 137 °C. The values of the two contact angles for higher temperatures are remarkably identical. For the SilverStone surface, the two angles are seen to be different in the temperature range investigated. It is not clear why the SilverStone surface exhibits such behavior.

The spreading of liquid upon impingement is another important factor. Kandlikar et al. [12] present the experimental results of spreading ratio as a function of Weber number and surface temperature on copper surface. A new correlation was developed to account for the contact angle effect on the spreading ratio.

3. Liquid–vapor interface behavior near critical heat flux condition

Dryout under a bubble, thin film formed by small nucleating bubbles, vapor cutback phenomenon. As seen from Figs. 3–6, the contact angles undergo a dramatic change as the surface temperature approaches 135–140 °C. Visual observations conducted by Kandlikar and Steinke [12,13] using two high speed video cameras confirm the initiation of transition boiling phenomenon at this temperature.

Kandlikar [2] developed a model for predicting the critical heat flux in pool boiling based on the contact line mechanism. The effect of the contact angle and the orientation was also included in his model. The model is based on a force balance on a bubble with rapidly evaporating interface close to CHF condition. Fig. 7 shows a schematic representation of the force balance used in their model. The resulting expression for the CHF is given below:

$$q''_{\mathrm{C}} = h_{fg}\rho_g^{1/2}\left(\frac{1+\cos\beta}{16}\right)\left[\frac{2}{\pi}+\frac{\pi}{4}(1+\cos\beta)\cos\phi\right]^{1/2} \times [\sigma g(\rho_l-\rho_g)]^{1/4}. \quad (1)$$

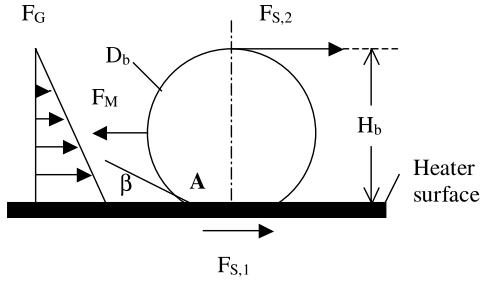

Fig. 7. Force balance on a vapor bubble growing in a liquid over a heated surface [2].

In deriving this expression, Kandlikar [2] proposed that the rapid evaporation occurring at the interface near the contact line region causes the liquid interface to retreat under the liquid creating a thin film of vapor. This mechanism leads to the CHF condition.

Fig. 8 shows a conceptual diagram depicting the movement of the liquid–vapor interface near the heater surface. The intense evaporation at the interface near the heater surface exerts a vapor recoil force pushing the interface into the liquid. The result is an increase in the contact angle as shown in Fig. 8. The motion of the liquid–vapor interface caused by a thin vapor film underneath the droplet is called as vapor cutback phenomenon. Since the interface is in motion due to evaporation, the contact angle at this condition represents the dynamic receding contact angle. This representation is in agreement with the jump in the receding contact angle seen in Figs. 4 and 5.

In an effort to validate this model, a high speed photographic study was conducted by Kandlikar and Steinke [13]. They used a copper heated surface that was polished using 1.0 μm alumina slurry. The heated surface had a surface roughness, R_a, value of 0.02 μm (average of five readings). The surface was then thoroughly cleaned several times using a DI water bath to remove any contaminants. Finally, the copper surface is heated in a vacuum furnace to dry the sample.

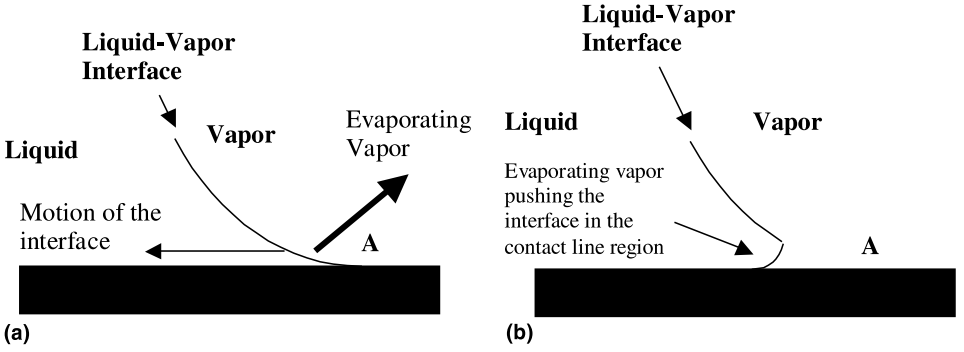

Fig. 8. Schematic representation of the contact line movement, or vapor cutback, resulting from vapor recoil forces.

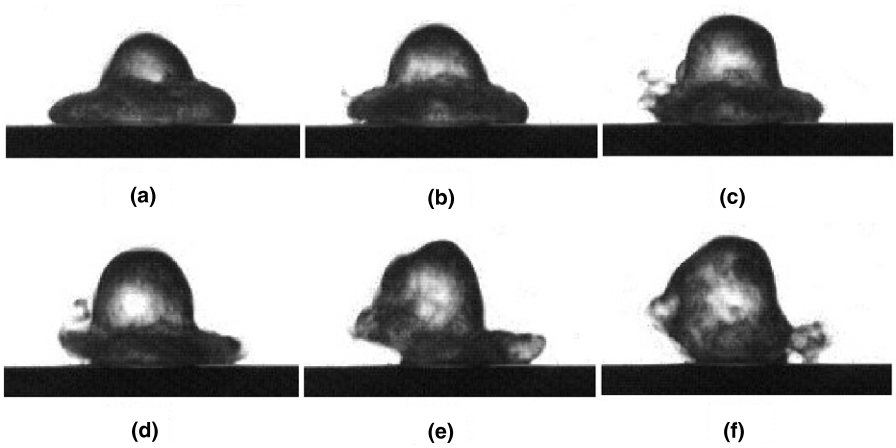

Fig. 9. Vapor cutback upon impact at the left side of the droplet, event time: (a) 0.0 ms, (b) 1.0 ms, (c) 2.0 ms, (d) 3.0 ms, (e) 4.0 ms, and (f) 5.0 ms. $T_w = 22$ °C, $T_s = 150$ °C, $d = 2.8$ mm.

The drop was placed on the heater surface using a droplet delivery system. The details of this system are same as those reported earlier while describing Figs. 3–6. The Weber number was calculated knowing the height through which the droplet falls on to the heater surface. A high speed video camera capable of taking pictures at a frame rate of 8000 frames per second was used to capture the digital video images.

A large number of images obtained under various conditions showed the vapor cutback phenomenon. Fig. 9 shows one such image sequence. Here the droplet in frame (a) is already experiencing a cutback phenomenon at its left edge. The change in the dynamic receding contact angle is seen as compared to the right edge of the droplet. In frame (b), the liquid has receded under the droplet leaving a wedge of vapor at the left edge. Small amount of liquid is also seen escaping with the evaporating vapor. This behavior continues through the rest of the frames. The right hand side edge also starts to experience the cutback phenomenon starting at frame (c). A small spray of liquid is also seen escaping from the right edge in frame (c). The movement of the interface near the contact line region continues, and the subsequent frame (d) shows this region extending deeper under

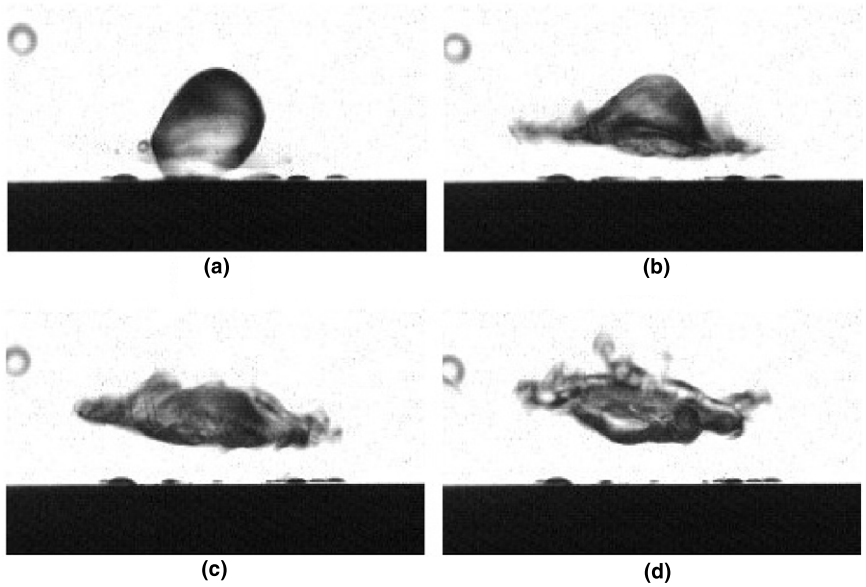

Fig. 10. Vapor cutback after droplet levitation, event time: (a) 0 ms, (b) 1.0 ms, (c) 2.0 ms, (d) 3.0 ms. $T_w = 22$ °C, $T_s = 175$ °C, $d = 2.8$ mm.

the liquid, with an increase in the contact angle. In frame (e), the heat flux is not high enough to support the further movement of the vapor underneath the liquid, and the contact angle is seen to decrease. Further movement of the interface is seen again in frame (f).

Another instance of the vapor cutback is seen in Fig. 10. Here the droplet is returning to the surface after bouncing off the first time. The heater surface is at a higher temperature than that shown in Fig. 9. As soon as the drop lands on the heater surface, vapor is generated underneath, perhaps on a nucleating cavity. The resulting bubble pushes the liquid vapor interface outwards, causing the droplet to float on a layer of vapor underneath. This behavior is believed to be due to vapor cutback that is pushing the liquid horizontally from underneath the droplet in the form of a liquid spray. This mechanism provides an explanation to the transition boiling phenomenon in which occasional contact of the liquid with the heater surface is followed by a burst of vapor leading to a temporary film boiling condition.

4. Liquid–vapor interface and contact line images of impinging droplets viewed through the bottom of a heated glass plate

The view of impinging droplets from underneath a heated glass surface provides valuable information

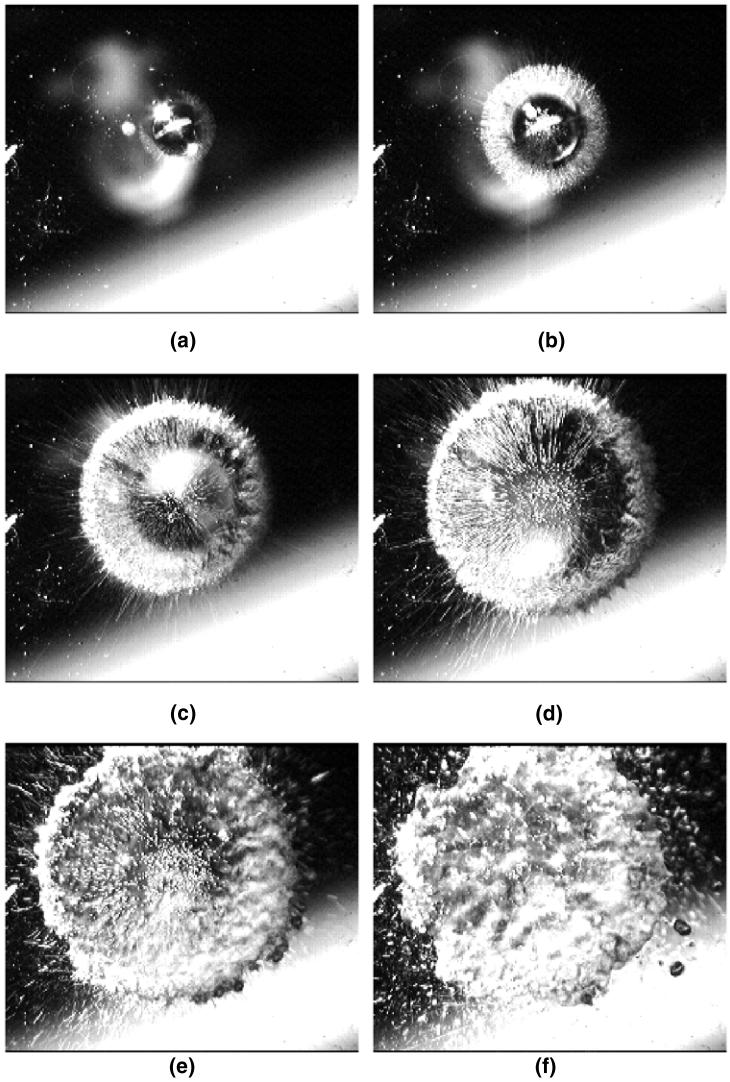

Fig. 11. Successive images of an impinging droplet going into transition boiling, viewed from the bottom of a heated glass plate, initial glass temperature = 220 °C. Image (a) at the instant of impact, $t = 0$ ms, (b) $t = 1$ ms, (c) $t = 3$ ms, (d) $t = 5$ ms, (e) $t = 9$ ms, (f) $t = 17$ ms.

regarding bubble nucleation, bubble interactions, and interface motion, especially near the CHF condition. Such experiments were carried out in the Thermal Analysis Laboratory at RIT. A special fire resistant glass that is designed to sustain water sprinklers under fire conditions was used in these tests.

The glass plate is supported on its edges by a stand and is heated with an annular ring heater of 25.4 mm inner diameter. This arrangement allows visual access from the bottom of the glass plate, while the drops can be dispensed on the top at the center of the annular heated region. The glass plate is heated to the desired initial temperature by adjusting the power input to the heater. A thermocouple is attached to the glass surface and is insulated from the surrounding air with a layer of high temperature epoxy. The temperature measurement provides only an approximate value as the transient temperature of the glass surface underneath the droplet is not measured. A high speed video camera with a microscopic lens attachment is positioned underneath the glass. The video images therefore provide information regarding the motion of interface and bubble interactions in the nucleate boiling, transition and film boiling regions as viewed from underneath the heated surface. These experiments were conducted in the air environment. Due to the presence of dissolved air in the impinging water droplets, nucleation is expected to occur sooner at lower surface temperatures. However, the

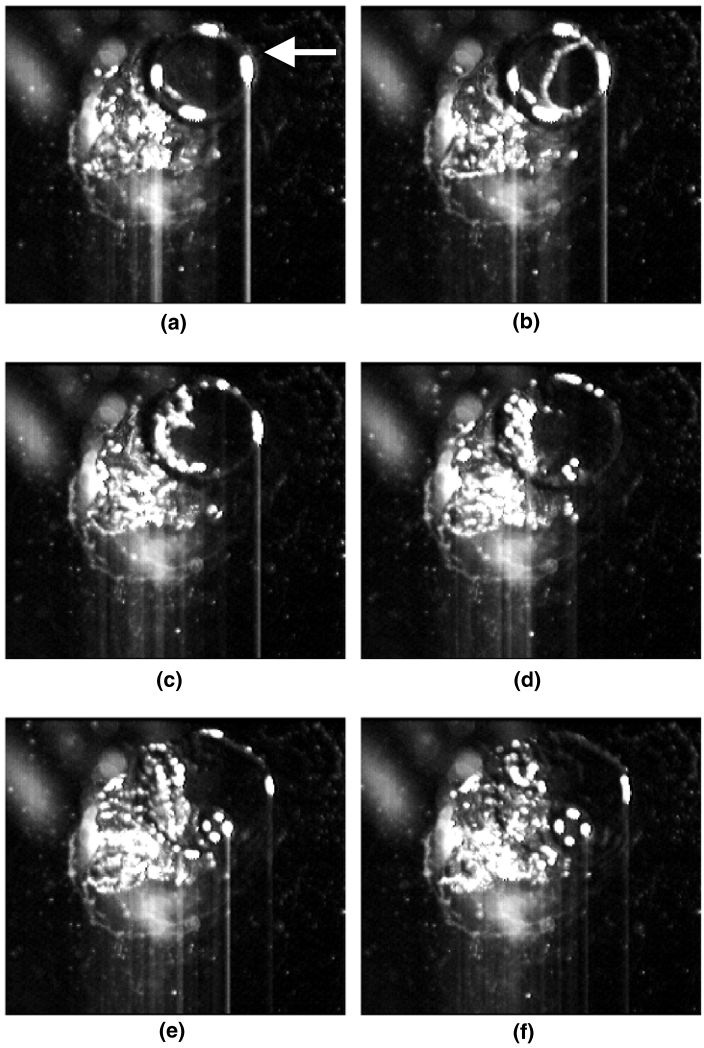

Fig. 12. Successive images of an impinging droplet undergoing dryout in the microlayer under a bubble, viewed from the bottom of a heated glass plate, initial glass temperature = 160 °C, Image (a) at the instant of impact, $t = 0$ ms, (b) $t = 1$ ms, (c) $t = 2$ ms, (d) $t = 3$ ms, (e) $t = 4$ ms, (f) $t = 5$ ms.

objective of these experiments was to obtain qualitative information regarding the motion of the interface, and to observe the dryout phenomenon. Further, following the intense transition boiling in many of the tests, the dissolved air content is expected to be extremely low in the liquid remaining on the heated surface.

Fig. 11 shows an image sequence with a droplet impinging on a horizontal heated glass plate at an initial temperature of 220 °C and a $We = 50$. Frame (a) shows the droplet at the instant of the impact on the glass surface (the images are 1 ms apart and the appearance of the contact in this frame indicates that the initial contact occurred during the 1 ms time interval between this and the previous frame). Intense nucleation is seen in the outer ring surrounding the central wetted region. Frames (b) and (c) show the spread of both the central region that is wetted by the liquid, and the annular region that is undergoing intense nucleate boiling activity. Nucleation is seen to occur in the entire region covered by the droplet in frame (d), captured 5 ms after frame (a). The individual bubbles grow and coalesce with the surrounding bubbles as seen in frame (e), captured 9 ms after the initial impact. Finally, frame (f), captured 17 ms after the initial impact, shows the violent breakup of the droplet with large vapor clusters forming underneath the bubble. The droplet at this stage is experiencing transition boiling in the entire region.

Fig. 12 shows an image sequence displaying the onset and propagation of a dryout patch in the layer underneath a bubble. The initial heater surface temperature is 180 °C, and $We = 50$. The droplet is undergoing transition boiling. The sequence shown begins 50 ms after the initial contact of the droplet with the heated surface.

Frame (a) in Fig. 12 shows an outline of the bubble base marked by four small reflected spots pointed out by an arrow. As mentioned earlier, the view is from the bottom of the horizontal glass plate looking through the bubble base. The video sequence was tracked prior to this frame, and it clearly showed the nucleation and growth of the bubble pointed out in frame (a). Frame (b) is taken 1 ms later. Here, a local dryout spot is seen to emerge in the liquid layer underneath the bubble. The dryout region is marked by the outline of a circular dryout front. The dryout front is touching the right side of the bubble base. In frame (c), the dryout front grows toward the left side of the bubble base. Since the wall temperature is not high enough, the liquid is seen creeping back as a film rewetting the dryout region from the lower left side. The liquid film continues to cover the bubble base in frames (d)–(f). In addition, another bubble is seen nucleating in the thin film region at the lower edge of the bubble in frame (d) marked by four bright reflections. The bubble continues to grow in frames (e) and (f).

The video sequence shown in Fig. 12 is indicative of how the dryout front progresses. At higher surface temperatures, the dryout front is expected to grow beyond the bubble base and exhibit the cutback phenomenon, leading to the CHF condition, as seen in Figs. 9 and 10 from the side views of the bubble.

The observations made in Fig. 12 validate the model proposed by Nikolayev and Beysens [16], who postulated that at CHF, a single dry spot under a bubble begins to spread. Although such spot is clearly seen in Figs. 12(b)–(f), the propagation of this front beyond the bubble base depends on the force balance at the base of the bubble. These forces depend on the recoil force, dynamic receding contact angle, surface tension, and orientation of the heater surface as proposed by Kandlikar [2].

5. Conclusions

The following conclusions are drawn from the work presented in this paper.

1. The equilibrium, advancing and receding contact angles are dependent on the surface roughness. For very smooth surfaces, the contact angle is seen to be higher for both copper and stainless steel surfaces. As the surface roughness is increased, the contact angles first decrease, but start increasing with increasing surface roughness.
2. The equilibrium contact angle lies between the static advancing and receding contact angle values. It depends on the history of the droplet on a given surface.
3. The dynamic advancing and receding contact angles of a moving liquid–vapor interface are different from the equilibrium advancing and receding contact angles.
4. The dynamic receding contact angle is seen to jump to the same value as the dynamic advancing contact angle at surface temperatures of 135–150 °C for water impinging on a heated stainless steel or copper surface. For the SilverStone® surface, no dramatic change is noticed in the dynamic receding contact angle over the range of temperatures investigated.
5. Vapor cutback phenomenon is postulated to be the mechanism responsible for the initiation of the CHF condition. Side views of a droplet impinging on a heated copper surface obtained using a high speed video camera at 1000 frames per second support this hypothesis.
6. High speed video images are obtained showing the formation of a dry spot and its subsequent propagation. At higher wall temperatures, the dryout front is believed to cut underneath the bulk liquid, as seen in the contact line cutback images depicted in Figs. 9 and 10. Very high speed photography (estimated to be on the order of 20,000–40,000 frames per second) is needed to clearly visualize the interface motion at CHF.

Acknowledgements

The work was conducted in the Thermal Analysis Laboratory at RIT. The support provided by the Rochester Institute of Technology is gratefully acknowledged.

References

[1] S.G. Kandlikar, Critical Heat Flux In Subcooled Flow Boiling – An Assessment of Current Understanding and Future Directions for Research, Keynote Lecture, Boiling 2000, Phenomena & Emerging Applications, in: Proceedings of the Engineering Foundation Conference, Anchorage, Alaska, April 30–May 5, 2000.

[2] S.G. Kandlikar, A Theoretical Model to Predict Pool Boiling CHF Incorporating Effects of Contact Angle and Orientation, Paper presented in the session on Fundamentals of Critical Heat Flux in Pool and Flow Boiling, in: ASME National Heat Transfer Conference, Pittsburgh, August 2000, ASME J. Heat Transfer 123 (2001) 1071–1079.

[3] F.C. Gunther, Photographic study of surface-boiling heat transfer to water with forced convection, Trans. ASME 73 (2) (1951) 115–123.

[4] F.E. Tippets, Critical heat fluxes and flow patterns in high pressure boiling water flows, ASME Paper 62-WA-162, ASME Winter Annual Meeting, ASME, New York, 1962.

[5] E.R. Hosler, Visual study of boiling at high pressure, AIChE Chem. Eng. Prog. Symp. Ser. 65 (57) (1965) 269–279.

[6] D.B. Kirby, J.R. Staniforth, J.H. Kinneir, A visual study of forced convection boiling, part I results for a flat vertical heater, UK Rep. AEEW-R-281, UK AEEW, Winfrith, England, 1965.

[7] L.S. Tong, H.B. Currin, P.S. Larsen, O.G. Smith, Influence of axially nonuniform heat flux on DNB, AIChE Symp. Ser. 62 (64) (1966) 35–40.

[8] L.S. Tong, Boiling Crisis and Critical Heat Flux, AEC Review Series, USAEC, Washignton, DC, 1972.

[9] S. Chandra, C.T. Avedisian, On the collision of a droplet with a solid surface, Proc. R. Soc. London A432 (1991) 13–41.

[10] S. Chandra, C.T. Avedisian, Observations of droplet impingement on a ceramic porous surface, Int. J. Heat Mass Transfer 35 (1992) 2377–2388.

[11] J.D. Bernardin, C.J. Stebbins, I. Mudawar, Mapping of impact and heat transfer regimes of water droplets impinging on a polished surface, Int. J. Heat Mass Transfer 40 (1997) 247–267.

[12] S.G. Kandlikar, M. Steinke, Contact angle of droplets during spread and recoil after impinging on a heated surface, IchemE Chemical Engineering Research and Design, April 2001.

[13] S.G. Kandlikar, M.E. Steinke, High speed photographic investigation of liquid–vapor interface and contact line movement during CHF and transition boiling, Paper No. 2-8-3-1, being presented at the ASME IMECE 2001, New York, 2001.

[14] S.G. Kandlikar, M.E. Steinke, A. Singh, Effects of Weber number and surface temperature on the boiling and spreading characteristics of impinging water droplets, Paper No. NHTC01-11672, in: Presented at the 35th National Heat Transfer Conference, Los Angeles, CA, June 10–12, 2001.

[15] S.G. Kandlikar, M.E. Steinke, S. Maruyama, T. Kimura, Molecular dynamics simulation and measurement of contact angle of water droplet on a platinum surface, Paper No. 2-8-3-2, being presented at the ASME IMECE 2001, New York, 2001.

[16] V.S. Nikolayev, D.A. Beysens, Boiling crisis and non-equilibrium drying transition, Europhys. Lett. 47 (3) (1999) 345–351.